Inter- and Intralayer Excitonic Spectrum of MoSe$_2$/WSe$_2$ Heterostructure

K. Sadecka*

Department of Theoretical Physics, Wrocław University of Science and Technology, Wybrzeże Wyspiańskiego 27, 50-370 Wrocław, Poland

         *e-mail: katarzyna.sadecka@pwr.edu.pl

Transition metal dichalcogenide heterostructures which are built from atomically thin layers of MX$_2$ crystals, enable the formation of excitons composed of electrons and holes in distinct layers. In the following work, we describe the electronic and excitonic properties of MoSe$_2$/WSe$_2$ heterostructure using a combination of the *ab initio* based effective mass approximation and the Bethe–Salpeter theory. First, we analyse electronic structure and Kohn–Sham wavefunctions that allow for spin/layer detection. In the next step, we construct an effective mass model for 8 bands around K valley consistent with experimental bandgaps. Using approximate inter- and intralayer screening we calculate the fine structure of inter- and intralayer excitons, predicting rich optical spectrum of interlayer A/B, spin bright/dark and ground/excited state with zero total momentum.

topics: excitons, transition metal dichalcogenides, heterostructures, Bethe-Salpeter equation

1. Introduction

Layered transition metal dichalcogenides (TMDs) with the chemical formula MX$_2$ (M = Mo, W; X = S, Se, Te) are novel semiconductor research platforms enabling the exploration of many fundamental physical phenomena related to their atomic thickness [1–4]. This includes, for example, low energy bands emulating massive Dirac fermion model, valley degrees of freedom which allow for selective excitation using circularly polarized light [5], strongly bound excitons [6], and robust charged exciton states [7–9] and more complicated excitonic molecules [10, 11]. Moreover, nontrivial topology of electronic bands may result in exciton fine structure renormalization [12, 13], peculiar response of valleys to magnetic fields [14] and broken symmetry valley-spin-polarized phases [15, 16].

TMDs are also the basic "blocks" for the construction of van der Waals heterostructures [17]. In such systems, e.g. MoSe$_2$/WSe$_2$ long-lived interlayer excitons composed of electrons and holes in distinct layers have been recently studied [18–31]. In such systems, it is possible to control the energy of interlayer excitons via gates [32, 33]. Moreover, the mutual twisting of layers [21, 34] can modify the exciton properties. The presence of moiré patterns [35] makes it possible to analyze the exotic properties of optical complexes in the presence of the moiré lattice potential [18, 21, 36, 37].

Description of the excitonic properties of TMD heterostructures is crucial in order to understand the optical response and analyse the charge carrier

dynamics. An accurate approach for electron–hole excitation calculations using density functional theory (DFT) must include both the quasiparticle self-energy corrections and the solution of the Bethe–Salpeter equation (BSE) [38], which allows the studies of exciton series [39–46]. In MoSe$_2$/WSe$_2$ heterostructure we deal with bright interlayer excitons with strong binding energies [42, 43]. Excitonic spectrum for twisted MoSe$_2$/WSe$_2$ was also studied [44, 46]. Interlayer exciton lifetime was calculated [44]. Due to the computationally challenging character of the DFT+GW+BSE method, effective approaches [47–52] have been used. The interlayer exciton binding energy of MoSe$_2$/WSe$_2$ for the 1s, 2s and 3s states was recently analysed using massive Dirac fermions model [50] and Wannier equation [53].

In this work, we begin by determining the electronic structure of MoSe$_2$/WSe$_2$, which allows us for the construction of effective mass approximation (EMA), with spin-resolved energy gaps estimated using experimental data. In the next step, the exciton fine structure determined by the type-II spin-split band arrangement is calculated, considering both A/B, spin bright/dark and intralayer/interlayer exciton series.

2. Theoretical model

We start with the electronic properties of the MoSe$_2$/WSe$_2$ heterostructure from the first principles. We consider the AB stacking where the metal atoms of one layer are localized under the chalcogen
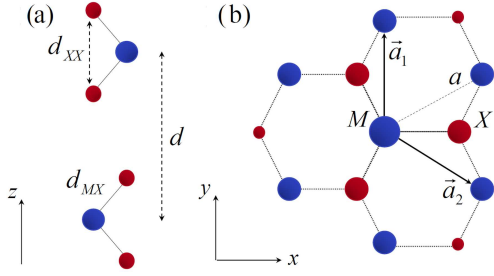
Fig. 1. (a) Side and (b) top view of an AB stacked MoSe$_2$/WSe$_2$ under the assumption of the same lattice constant a. Both metal atoms are represented in blue, and chalcogen atoms are in red. In plane lattice parameter $a = 3.288$ Å, chalcogen atoms distance $d_{XX} = 2.52$ Å, and metal-chalcogen distance is $d_{MX} = 3.33$ Å, following [54]. Interlayer distance is set to $d = 6.4$ Åas discussed in text.

TABLE I

Determined effective masses m^* (m_0), where m_0 is the free electron mass, for 4 VB and 4 CB around the K valley for the MoSe$_2$/WSe$_2$ structure.

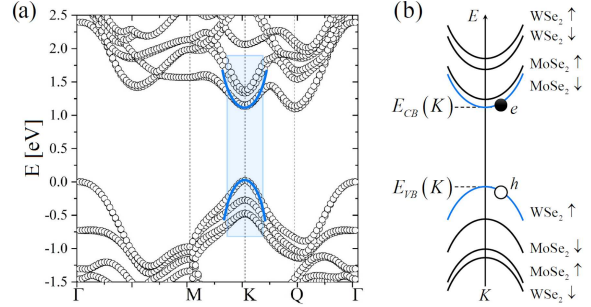| Band index	CB	CB + 1	CB + 2	CB + 3
m_e^* (m_0)	0.62	0.51	0.55	0.34
Band index	VB − 3	VB − 2	VB − 1	VB
m_h^* (m_0)	0.48	0.55	0.37	0.27

Fig. 2. (a) DFT band structure of a MoSe$_2$/WSe$_2$ heterostructure with schematic representation of the parabolic model. (b) A scheme of the electronic structure in effective mass approximation for 4 valence bands and 4 conduction bands with the layer and spin characterization for each band.

atoms of the other layer, as depicted in Fig. 1a. The honeycomb lattice of the system is presented in the top view in Fig. 1b. Lattice vectors are defined as $\boldsymbol{a}_1 = (0, a)$ and $\boldsymbol{a}_2 = (a\sqrt{3}/2, -a/2)$, where $a = d_{MM}$ is the lattice constant, as presented in Fig. 1b. We note that the lattice mismatch in MoSe$_2$/WSe$_2$ is negligibly small ($\Delta a < 0.01$ Å), so no significant stresses occur. In order to determine interlayer distance d, the total energy as a function of layers distance was analysed, following [54], and the energy minimum was obtained for $d = 6.4$ Å. Energies and wavefunctions of the MoSe$_2$/WSe$_2$ were calculated from the first principles implemented in Abinit [55] code using the Perdew–Burke–Ernzerhof (PBE) exchange-correlation (XC) energy functional [56] and the projector augmented wave method (PAW) [57]. Van der Waals interactions have been taken into account according to the DFT–D3 XC functional [58]. The PBE parametrization was used with a plane-wave cutoff of 120 Ha, the energy cutoff of 60 Ha, and a $12 \times 12 \times 1$ k-point mesh. All calculations included the spin–orbit coupling (SOC). Vacuum between the primitive cells along z-direction has been set to 20 Å. According to our calculations, MoSe$_2$/WSe$_2$ is characterized by an indirect band gap K–Q as presented in Fig. 1a, in contrast to a direct gap of the distinct MoSe$_2$ and WSe$_2$ monolayers.

In next step, we performed layer and spin symmetries detection. Kohn–Sham wavefunctions can be described as $\psi_{\boldsymbol{k}}^n (\boldsymbol{r}, \sigma) = \mathrm{e}^{\mathrm{i}\boldsymbol{k}\cdot\boldsymbol{r}} u_{\boldsymbol{k}}^n (\boldsymbol{r}, \sigma)$, where n is the band index, $\sigma = \{\uparrow, \downarrow\}$ denotes spin, and $u_{\boldsymbol{k}}^n (\boldsymbol{r}, \sigma)$ describes a periodic function in plane-wave representation $u_{\boldsymbol{k}}^n (\boldsymbol{r}, \sigma) = \sum_{\boldsymbol{G}} c_{\boldsymbol{k}}^n (\boldsymbol{G}, \sigma) \mathrm{e}^{\mathrm{i}\boldsymbol{k}\cdot\boldsymbol{G}}$. Here, $\boldsymbol{G}$ is the reciprocal space vector. In order to analyse the spin and layer symmetries, we consider the density ρ defined as $\rho^{\uparrow(\downarrow)}(z) = \iint_{UC} \mathrm{d}x\, \mathrm{d}y\, \left|\psi^{\uparrow(\downarrow)}(x, y, z)\right|^2$, where UC denotes the unit cell. The study of the density ρ as a function of the z-axis position allows to determine the

leading layer and spin contribution for a given band and k-point from the Brillouin zone. Next, the effective masses m^* of electron and hole for 8 energy bands around the direct (K–K) energy gaps of the MoSe$_2$/WSe$_2$ heterostructure were determined, according to the relation $E_n = E_n(K) \pm \frac{\hbar^2 \nabla^2}{2m_n^*}$, where $m_n^* > 0$ and E_n denotes max / min for one of the 4 considered valence/conduction bands, as shown in Fig. 2b and described in Table I.

In order to obtain both intra- and interlayer exciton fine structures in EMA, we solve [38] BSE equation without small, screened electron–hole exchange interaction [6], i.e.,

$$\left(\Delta E_{\boldsymbol{k}} - \Delta_{\mathrm{GAP}}\right) A_{n,\boldsymbol{k}} - \sum_{\boldsymbol{k'}} V_{\boldsymbol{k},\boldsymbol{k'}} A_{n,\boldsymbol{k'}} = E_n A_{n,\boldsymbol{k}}, \tag{1}$$

where $\Delta E(\boldsymbol{k})$ is the energy between chosen CB and VB (depending on studying optical transition type) in EMA for given k-point. The corresponding energy gap $\Delta_{\mathrm{GAP}} = E_{n_1}(K) - E_{n_2}(K)$ was estimated using the first principles electronic structure calculations and experimental results presented in [18, 59], under assumption that spin-splittings known from GGA level are not affected by many-body corrections. Specifically, we extract experimental [18] position of $1s$ excitonic ground state with respect to valence band energy given by GGA for intra-layer excitons. In second step

we add binding energies of hexagonal boron nitride (hBN) encapsulated samples estimated precisely in the magnetic field — type experiment in [59]. This information, combined with the band-offset and spin-splitting predicted from GGA, gives experimentally based band edges that are used in further calculations. The values of the energy differences in K point necessary in order to determine Δ_{GAP} for all n_1 and n_2 combinations, as presented in Fig. 2, are $E_{\text{CB}} - E_{\text{VB}} = 1527$ meV, $E_{\text{CB}+3} - E_{\text{CB}+1} = 360$ meV, and $E_{\text{VB}} - E_{\text{VB}-1} = 358$ meV, respectively. All spin-splittings are $\Delta_{\text{SOC}} = 506$ meV for WSe_2^{VB}, $\Delta_{\text{SOC}} = 198$ meV for $\text{MoSe}_2^{\text{VB}}$, $\Delta_{\text{SOC}} = 43$ meV for WSe_2^{CB} and $\Delta_{\text{SOC}} = 21$ meV for $\text{MoSe}_2^{\text{CB}}$, respectively. In (1), $A_n(\boldsymbol{k})$ are the exciton wavefunctions and $V(\boldsymbol{k}, \boldsymbol{k}')$ describes the direct electron–hole Coulomb interactions. Slow scaling with increasing discretization of the Brillouin zone makes it computationally challenging to obtain numerical BSE solutions with high accuracy. We perform the exciton spectrum calculations with large k-point sampling, approximately 10^5 k-points per valley. This allows for a discussion of energetic position of $1s$, $2s$ and $2p$ states in a computationally converged manner.

An important aspect of the exciton fine structure calculations is the effect of the non-local Coulomb interactions [60, 61]. In the following work we use the Rytova–Keldysh screening model [62, 63]. Specifically, we study the case of $\text{MoSe}_2/\text{WSe}_2$ encapsulated in the hexagonal boron nitride (hBN). Following the model by Ovesen et al. [53] assuming $qd \ll 1$, where $q = |\boldsymbol{k}' - \boldsymbol{k} - \boldsymbol{G}|$ and where $\boldsymbol{G}$ minimalizes the $|\boldsymbol{k}' - \boldsymbol{k}|$ distance, we determine the dielectric function for intra- and interlayer screening as

$$\varepsilon^{l_{1,2}}(k) \approx \varepsilon - \frac{dq}{\varepsilon_{l_1}\varepsilon_{l_2}}\left(\varepsilon_{l_1} + \varepsilon_{l_2}\right)\left(\varepsilon^2 - \varepsilon_{l_1}\varepsilon_{l_2}\right), \tag{2}$$

and

$$\varepsilon^{l_1,l_2}(k) \approx \varepsilon - \frac{dq}{2}\left(\varepsilon_{l_1} + \varepsilon_{l_2}\right), \tag{3}$$

respectively. We note that in (2) and (3) the quantity $\varepsilon = (\varepsilon_1 + \varepsilon_2)/2 = \varepsilon_{\text{hBN}} = \varepsilon_r^{\text{R-K}} = 4.5$ describes static Rytova–Keldysh screening of the surrounding material. One can rewrite (2) and (3) in the form of

$$\varepsilon^{l_{1,2}/l_1,l_2}(k) = \varepsilon_r^{\text{R-K}}\left(1 + \alpha_{\text{Keldysh}}^{\text{intra/inter}}q\right), \tag{4}$$

where $\alpha_{\text{Keldysh}}^{\text{intra/inter}}$ can be treated as parameters. Their values are important in order to correctly determine the experimentally known $1s$-state energies for both intra- and interlayer excitons. Following [59] we take the ground state of the intralayer excitons $E_{n=1}^{\text{WSe}_2} = 167$ meV and $E_{n=1}^{\text{MoSe}_2} = 231$ meV, while for the interlayer exciton $E_{n=1} = 150$ meV as determined in [18]. Parameters of screening for assumed $1s$-state energies are $\alpha_{\text{Keldysh}}^{\text{intra,WSe}_2} = 1.34$, $\alpha_{\text{Keldysh}}^{\text{intra,MoSe}_2} = 1.21$, and $\alpha_{\text{Keldysh}}^{\text{inter}} = 2.30$, respectively. Determination of the bright $1s$-state energies for both intra- and interlayer excitons by setting

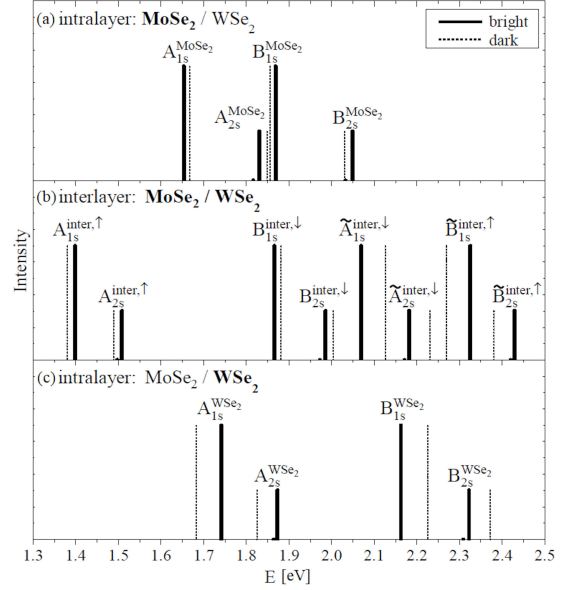
Fig. 3. Theoretically predicted optical transition energies for $1s$ and $2s$-states in $\text{MoSe}_2/\text{WSe}_2$ heterostructure for (a) intralayer excitons in MoSe_2 layer, (b) interlayer excitons and (c) intralayer excitons in WSe_2 layer. Continuous and dashed lines represent spin-bright and -dark states, respectively. For interlayer excitons, excitons built from hole WSe_2 and electron in MoSe_2 layer (electron in MoSe_2 and hole in WSe_2) are denoted as $A^{\text{inter},\uparrow}$ and $B^{\text{inter},\downarrow}$ ($\tilde{A}^{\text{inter},\downarrow}$ and $\tilde{B}^{\text{inter},\uparrow}$). The spin symbol ($\uparrow$ and $\downarrow$) was introduced for bright excitons only. The absorption intensity was marked in a schematic manner only to distinguish between $1s$ and $2s$-states.

the screening parameters giving them values following [18, 59] allows us to obtain results staying in good agreement with experimentally known optical transition energies of $\text{MoSe}_2/\text{WSe}_2$ heterostructure [18, 33].

3. Excitonic spectrum

In the next step, we solve BSE given in (1) using various spin-split combinations of bands, allowing to study the fine structure of the exciton spectrum of the $\text{MoSe}_2/\text{WSe}_2$ heterostructure at K point for excitons with zero total momentum. In Fig. 3, we consider A/B, spin bright/dark and intra-/interlayer exciton series of $\text{MoSe}_2/\text{WSe}_2$ in accordance with Fig. 2b, restricting ourselves to $1s$ and $2s$ states.

Figure 3 shows optical spectrum of the $\text{MoSe}_2/\text{WSe}_2$ system restricted to $1s$ and $2s$ states only. The exciton series, presented as the absorption intensity bars, are shown separately for intralayer excitons (for both MoSe_2 and WSe_2 layers) in Fig. 3a and c and for interlayer excitons in Fig. 3b. The distinction of spin-bright (denoted

Summary of the bright A–B and $1s$–$2s$ energy splittings for different combinations of optical transitions. All values are represent in [eV].

Exciton type	intra- / MoSe$_2$	intra- / WSe$_2$	interlayer
$\Delta^{1s/2s}$(A–B)	0.21 / 0.21	0.42 / 0.45	0.47 / 0.48
$\Delta^{1s/2s}$(Ã–B̃)	–	–	0.26 / 0.25
$\Delta^{\mathrm{A/B}}(1s-2s)$	0.18 / 0.18	0.13 / 0.16	0.11 / 0.12
$\Delta^{\tilde{\mathrm{A}}/\tilde{\mathrm{B}}}(1s-2s)$	–	–	0.11 / 0.10

with continous lines) and -dark states (dashed lines) was also introduced. The intensity of the excited states ($2s$) is lower than for the ground state ($1s$), which was denoted in an approximate in Fig. 3 way in order to illustrate the differences in the contribution of individual excitonic states to the optical response of the heterostructure. Quantitatively, $2s$-state intensity relative to $1s$-state can be determined on the basis of the Elliott formula [64, 65] to be about 20%.

Based on energies of the bright $1s$ states for both intra- and interlayer excitons, as described in Sect. 2, for energy window 1.3–1.8 eV, we obtain results consistent with the experimentally known intra- and interlayer exciton series of MoSe$_2$/WSe$_2$ [18, 20, 22–31, 33], namely $E_{1s}^{\mathrm{MoSe_2}} = 1.67$ eV, $E_{1s}^{\mathrm{WSe_2}} = 1.74$ eV and $E_{1s}^{\mathrm{inter}} = 1.40$ eV. For intralayer excitons, those energies are almost unaffected by the presence of the second layer, representing the values characteristic for monolayer MoSe$_2$ and WSe$_2$ [66–68]. Considering both A/B exciton types for bright $1s$ and $2s$ states, we can analyse the A–B and $1s$–$2s$ splittings. All obtained values are presented in Table II.

Analysing intralayer excitons only we are able to notice that mutual arrangement of bright and dark s-states, known from analyzes of isolated monolayers [66–68], is preserved. For the MoSe$_2$, the layer bright A$_{1s}$ state (similarly A$_{2s}$) is energetically lower than the dark one, while for WSe$_2$ layer, the energetic arrangement of states is reversed as presented in Fig. 3a and c. Additionally, the energy difference between bright and dark state is bigger for the WSe$_2$ layer. For the interlayer excitons, the structure of bright and dark states becomes more complicated. This effect is shown in Fig. 3b. For optical transitions from WSe$_2$ to MoSe$_2$ layer, denoted as A$^{\mathrm{inter},\uparrow}$ and B$^{\mathrm{inter},\downarrow}$, the energy distribution of bright and dark states is similar to the case of the intralayer excitons for WSe$_2$ layer. In turn, the energetic positions of Ã$^{\mathrm{inter},\downarrow}$ and B̃$^{\mathrm{inter},\uparrow}$ states (transitions from MoSe$_2$ to WSe$_2$) correspond to the distribution of bright and dark states for MoSe$_2$ layer. This arrangement for the energetically lowest transitions stays in good agreement with the experimental observations [27].

While the intralayer exciton series for both MoSe$_2$ and WSe$_2$ remain almost unaffected by the second layer keeping the optical spectrum characteristic for monolayers, the states from distinct layers present a rich spectrum of different types of interlayer excitons. Considering not only the energetically lowest optical transitions (A$^{\mathrm{inter},\uparrow}$), but also higher energy window as well (1.8–2.5 eV), we predict the presence of additional lines coming from interlayer B$^{\mathrm{inter},\downarrow}$, Ã$^{\mathrm{inter},\downarrow}$ and B̃$^{\mathrm{inter},\uparrow}$ excitons for both bright and dark optical transition types. Up to our knowledge, this rich interlayer exciton series was experimentally unobserved yet.

4. Conclusions

We presented here an *ab initio* based theory of excitons in a TMD heterostructures. The electronic properties of MoSe$_2$/WSe$_2$ were first analysed using DFT methods. We performed the detection of layer and spin symmetries using DFT Kohn–Sham wavefunctions and determined the effective masses of electron and hole for 8 energy bands around the K valley. Using effective mass approximation for the spin-split bands and using the Rytova–Keldysh screening with parameters set to reproduce experimentally known $1s$-states, we solved the BSE with high accuracy in order to obtain intra- and interlayer exciton fine structure. We considered both A and B, and spin bright and dark exciton series, predicting rich variety of interlayer optical transitions.

Acknowledgments

References

[1] A. Splendiani, L. Sun, Y. Zhang, T. Li, J. Kim, C.-Y. Chim, G. Galli, F. Wang, *Nano Lett.* **10**, 1271 (2010).

[2] K.F. Mak, C. Lee, J. Hone, J. Shan, T.F. Heinz, *Phys. Rev. Lett.* **105**, 136805 (2010).

[3] G. Wang, A. Chernikov, M.M. Glazov, T.F. Heinz, X. Marie, T. Amand, B. Urbaszek, *Rev. Mod. Phys.* **90**, 021001 (2018).

[4] E.S. Kadantsev, P. Hawrylak, *Solid State Commun.* **152**, 909 (2012).

[5] D. Xiao, G.-B. Liu, W. Feng, X. Xu, W. Yao, *Phys. Rev. Lett.* **108**, 196802 (2012).

[6] M. Bieniek, L. Szulakowska, P. Hawrylak, *Phys. Rev. B* **101**, 125423 (2020).

[7] J. Jadczak, J. Kutrowska-Girzycka, P. Kapuściński, Y.S. Huang, A. Wójs, L. Bryja, *Nanotechnology* **28**, 395702 (2017).

[8] J. Jadczak, L. Bryja, J. Kutrowska-Girzycka, P. Kapuściński, M. Bieniek, Y.-S. Huang, P. Hawrylak, *Nat. Commun.* **10**, 1 (2019).

[9] J. Jadczak, J. Kutrowska-Girzycka, M. Bieniek, T. Kazimierczuk, P. Kossacki, J.J. Schindler, J. Debus, K. Watanabe, T. Taniguchi, C.H. Ho, A. Wójs, P. Hawrylak, L. Bryja, *Nanotechnology* **32**, 145717 (2021).

[10] Y. You, X.-X. Zhang, T.C. Berkelbach, M.S. Hybertsen, D.R. Reichman, T.F. Heinz, *Nat. Phys.* **11**, 477 (2015).

[11] M. Zinkiewicz, T. Woźniak, T. Kazimierczuk et al., *Nano Lett.* **21**, 2519 (2021).

[12] A. Srivastava, A. Imamoğlu, *Phys. Rev. Lett.* **115**, 166802 (2015).

[13] J. Zhou, W.-Y. Shan, W. Yao, D. Xiao, *Phys.Rev. Lett.* **115**, 166803 (2015).

[14] M. Bieniek, M. Korkusiński, L. Szulakowska, P. Potasz, I. Ozfidan, P. Hawrylak, *Phys. Rev. B* **97**, 085153 (2018).

[15] T. Scrace, Y. Tsai, B. Barman, L. Schweidenback, A. Petrou, G. Kioseoglou, I. Ozfidan, M. Korkusiński, P. Hawrylak, *Nat. Nano.* **10**, 603 (2015).

[16] L. Szulakowska, M. Cygorek, M. Bieniek, P. Hawrylak, *Phys. Rev. B* **102**, 245410 (2020).

[17] A.K. Geim, I.V. Grigorieva, *Nature* **499**, 419 (2013).

[18] P. Rivera, J.R. Schaibley, A.M. Jones, J.S. Ross, S. Wu, G. Aivazian, P. Klement, K. Seyler, G. Clark, N.J.Ghimire, J. Yan, D.G. Mandrus, W. Yao, X. Xu, *Nat. Commun.* **6**, 1 (2015).

[19] P. Rivera, K.L. Seyler, H. Yu, J.R. Schaibley, J. Yan, D.G. Mandrus, W. Yao, X. Xu, *Science* **351**, 688 (2016).

[20] B. Miller, A. Steinhoff, B. Pano, J. Klein, F. Jahnke, A. Holleitner, U. Würstbauer, *Nano Lett.* **17**, 5229 (2017).

[21] J. Choi, M. Florian, A. Steinhoff et al., *Phys. Rev. Lett.* **126**, 047401 (2021).

[22] P. Nagler, M.V. Ballottin, A.A. Mitioglu et al., *Nat. Commun.* **8**, 1 (2017).

[23] W.-T. Hsu, L.-S. Lu, P.-H. Wu, M.-H. Lee, P.-J. Chen, P.-Y. Wu, Y.-C. Chou, H.-T. Jeng, L.-J. Li, M.-W. Chu, W.-H. Chang, *Nature Commun.* **9**, 1 (2018).

[24] A.T. Hanbicki, H.-J. Chuang, M.R. Rosenberger, C.S. Hellberg, S.V. Sivaram, K.M. McCreary, I.I. Mazin, B.T. Jonker, *ACS Nano* **12**, 4719 (2018).

[25] J. Wang, J. Ardelean, Y. Bai, A. Steinhoff, M. Florian, F. Jahnke, X. Xu, M. Kira, J. Hone, X.-Y. Zhu, *Sci. Adv.* **5**, eaax0145 (2019).

[26] A. Ciarrocchi, D. Unuchek, A. Avsar, K. Watanabe, T. Taniguchi, A. Kis, *Nat. Photonics* **13**, 131 (2019).

[27] T. Wang, S. Miao, Z. Li, Y. Meng, Z. Lu, Z. Lian, M. Blei, T. Taniguchi, K. Watanabe, S. Tongay, D. Smirnov, S.-F. Shi, *Nano Lett.* **20**, 694 (2019).

[28] L. Zhang, R. Gogna, G.W. Burg, J. Horng, E. Paik, Y.-H. Chou, K. Kim, E. Tutuc, H. Deng, *Phys. Rev. B* **100**, 041402 (2019).

[29] W. Li, X. Lu, S. Dubey, L. Devenica, A. Srivastava, *Nat. Mater.* **19**, 624 (2020).

[30] A.Y. Joe, L.A. Jauregui, K. Pistunova et al., *Phys. Rev. B* **103**, L161411 (2021).

[31] L. Sigl, F. Sigger, F. Kronowetter, J. Kiemle, J. Klein, K. Watanabe, T. Taniguchi, J. J. Finley, U. Wurstbauer, A.W. Holleitner, *Phys. Rev. Res.* **2**, 042044 (2020).

[32] E. Calman, M. Fogler, L. Butov, S. Hu, A. Mishchenko, A. Geim, *Nat. Commun.* **9**, 1 (2018).

[33] L.A. Jauregui, A.Y. Joe, K. Pistunova et al., *Science* **366**, 870 (2019).

[34] E.M. Alexeev, D.A. Ruiz-Tijerina, M. Danovich et al., *Nature* **567**, 81 (2019).

[35] K. Tran, J. Choi, A. Singh, *2D Materials* **8**, 022002 (2020).

[36] K.L. Seyler, P. Rivera, H. Yu, N.P. Wilson, E.L. Ray, D.G. Mandrus, J. Yan, W. Yao, X. Xu, *Nature* **567**, 66 (2019).

[37] M. Brotons-Gisbert, H. Baek, A. Campbell, K. Watanabe, T. Taniguchi, B.D. Gerardot, *Phys.Rev. X* **11**, 031033 (2021).

[38] M. Rohlfing, S.G. Louie, *Phys. Rev. B* **62**, 4927 (2000).

[39] A. Molina-Sánchez, D. Sangalli, K. Hummer, A. Marini, L. Wirtz, *Phys. Rev. B* **88**, 045412 (2013).

[40] J. He, K. Hummer, C. Franchini, *Phys. Rev. B* **89**, 075409 (2014).

[41] S. Gao, L. Yang, C. D. Spataru, *Nano Lett.* **17**, 7809 (2017).

[42] R. Gillen, J. Maultzsch, *Phys. Rev. B* **97**, 165306 (2018).

[43] E. Torun, H.P. Miranda, A. Molina-Sánchez, L. Wirtz, *Phys. Rev. B* **97**, 245427 (2018).

[44] X. Lu, X. Li, L. Yang, *Phys. Rev. B* **100**, 155416 (2019).

[45] H. Guo, X. Zhang, G. Lu, *Sci. Adv.* **6**, eabc5638 (2020).

[46] Z. Li, X. Lu, D.F. Cordovilla Leon et al., *ACS Nano* **15**, 1539 (2021).

[47] A. Arora, M. Koperski, A. Slobodeniuk et al., *2D Materials* **6**, 015010 (2018).

[48] A.O. Slobodeniuk, L. Bala, M. Koperski et al., *2D Materials* **6**, 025026 (2019).

[49] S. Das, G. Gupta, K. Majumdar, *Phys. Rev. B* **99**, 165411 (2019).

[50] M. Van der Donck, F. Peeters, *Phys. Rev. B* **98**, 115104 (2018).

[51] P. Merkl, F. Mooshammer, P. Steinleitner et al., *Nat. Mater.* **18**, 691 (2019).

[52] O.L. Berman, R.Y. Kezerashvili, *Phys. Rev. B* **96**, 094502 (2017).

[53] S. Ovesen, S. Brem, C. Linderälv, M. Kuisma, T. Korn, P. Erhart, M. Selig, E. Malic, *Commun. Phys.* **2**, 1 (2019).

[54] J. He, K. Hummer, C. Franchini, *Phys. Rev. B* **89**, 075409 (2014).

[55] X. Gonze, J.-M. Beuken, R. Caracas et al., *Comput. Mater. Sci.* **25**, 478 (2002).

[56] J.P. Perdew, K. Burke, M. Ernzerhof, *Phys. Rev. Lett.* **77**, 3865 (1996).

[57] P. E. Blöchl, *Phys. Rev. B* **50**, 17953 (1994).

[58] S. Grimme, J. Antony, S. Ehrlich, H. Krieg, *J. Chem. Phys.* **132**, 154104 (2010).

[59] S. Crooker, M. Goryca, J. Li et al., *Nat. Commun.* **10**, 4172 (2019).

[60] P. Cudazzo, I.V. Tokatly, A. Rubio, *Phys. Rev. B* **84**, 085406 (2011).

[61] A. Chernikov, T.C. Berkelbach, H.M. Hill, A. Rigosi, Y. Li, O.B. Aslan, D.R. Reichman, M.S. Hybertsen, T.F. Heinz, *Phys. Rev. Lett.* **113**, 076802 (2014).

[62] N.S. Rytova, *Proc. MSU, Phys. Astron.* **3**, 30 (1967).

[63] L. Keldysh, *Sov. J. Exp. Theor. Phys. Lett.* **29**, 658 (1979).

[64] R.J. Elliott, *Phys. Rev.* **108**, 1384 (1957).

[65] T.C. Berkelbach, M.S. Hybertsen, D.R. Reichman, *Phys. Rev. B* **92**, 085413 (2015).

[66] X.-X. Zhang, T. Cao, Z. Lu et al., *Nat. Nanotechnol.* **12**, 883 (2017).

[67] M.R. Molas, A.O. Slobodeniuk, T. Kazimierczuk et al., *Phys. Rev. Lett.* **123**, 096803 (2019).

[68] C. Robert, B. Han, P. Kapuściński et al., *Nat. Commun.* **11**, 1 (2020).